Lab on a Chip

Dynamic Article Links

Cite this: *Lab Chip*, 2012, **12**, 4403–4415

www.rsc.org/loc

PAPER

Optofluidic microsystems with integrated vertical one-dimensional photonic crystals for chemical analysis†

S. Surdo,[a] S. Merlo,[b] F. Carpignano,[b] L. M. Strambini,[a] C. Trono,[c] A. Giannetti,[c] F. Baldini[c] and G. Barillaro*[a]

Received 28th May 2012, Accepted 6th August 2012
DOI: 10.1039/c2lc40613f

In this work, we report all-silicon, integrated optofluidic microsystems (OFMs) fabricated by electrochemical micromachining (ECM) technology, in which high aspect-ratio (HAR) photonic crystal (PhC) devices (*i.e.* micromirrors, optical cavities) are integrated by one-etching-step, together with microfluidic reservoirs/channels, for the infiltration of liquids in the PhC air gaps, and with fiber grooves for alignment/positioning of readout optical fibers in front of the PhC, on the same silicon die. This has not previously been reported in the literature, and opens up new ground in, though not limited to, the optofluidics field, due to the low-cost and high-flexibility of the ECM technology that allows optofluidic microsystem fabrication to be performed in any lab. Optofluidic characterization of PhC-OFMs by both capillary-action and pressure-driven operations is carried out through the measurement of the reflectivity spectra of HAR-PhCs upon injection of liquids featuring different refractive index values in the HAR-PhC air gaps, by using readout optical fibers positioned in the on-chip fiber grooves. High sensitivity and good limit of detection of PhC-OFMs are obtained for both capillary-action and pressure-driven operations. A best sensitivity value of 670 nm/RIU and a worst-case limit of detection of the order of 10^{-3} RIU are measured, the former being comparable to state-of-the-art integrated refractive index sensors and the latter being limited by constraints of the experimental setup. The proof of concept about the biosensing potential of PhC-OFMs is given by successfully carrying out a sandwich assay based on antigen–antibody interactions for the detection of the C-reactive protein (CRP) at a concentration value of 10 mg L^{-1}, which represents the boundary level between physiological and pathological conditions.

Introduction

There is an increasing research trend for the fabrication of a novel generation of optofluidic microsystems (OFMs) for label-free biological/chemical analysis that integrate materials with unique optical properties in microfluidic systems, among which photonic crystals are an example.[1–4]

Photonic crystals (PhCs) are artificial or natural micro/nano-structures characterized by spatial, periodic arrangement of dielectric materials with sufficiently high refractive index contrast in one (1D), two (2D), or three (3D) dimensions.[5,6] PhCs have been a subject of great interest in the materials science community for many years, thanks to their unique characteristic of featuring a photonic bandgap (PBG) that allows the manipulation of light propagation at a sub-wavelength scale to be effectively performed.[7–10] PhCs have been successfully used for a broad range of applications, including optoelectronics,[11] photocatalysis,[12] photovoltaics[12] and displays.[13]

More recently, PhCs have attracted great attention in the field of biological/chemical analysis for label-free sensors that exploit the high sensitivity of PhC optical properties to tiny changes of the dielectric constant and/or thickness of the composing materials upon interaction of the PhC with the analyte/fluid to be identified.[2,14] Integration of such PhC structures into microfluidic networks has lead to the first generation of photonic crystal optofluidic microsystems (PhC-OFMs),[1,15–17] in which planar PhCs characterized by a reduced value of the aspect-ratio (height-to-width ratio smaller than or about 1) are employed to monitor changes of PhC optical properties induced by light-matter interaction of analytes/fluids with the PhC structure at a surface level. High sensitivity and a good limit of detection have been experimentally demonstrated for such a first generation of label-free PhC-OFMs for both biological and chemical analyses. However, though a number of different architectures have been proposed for increasing light–matter interaction at the PhC

[a]*Dipartimento di Ingegneria dell'Informazione: Elettronica, Informatica, Telecomunicazioni, Università di Pisa, via G, Caruso 16, 56126, Pisa, Italy. E-mail: g.barillaro@iet.unipi.it; Fax: +39 050 2217 522; Tel: +39 050 2217 601*
[b]*Dipartimento di Ingegneria Industriale e dell'Informazione, Università di Pavia, Via Ferrata 1, 27100, Pavia, Italy. E-mail: sabina.merlo@unipv.it; Fax: +39 0382 422586; Tel: +39 0382 985202*
[c]*Istituto di Fisica Applicata "Nello Carrara"-CNR Via Madonna del Piano 10, 50019, Sesto Fiorentino, Firenze, Italy. E-mail: f.baldini@ifac.cnr.it; Fax: +39 055 5226359; Tel: +39 055 5226400*

† Electronic supplementary information (ESI) available. See DOI: 10.1039/c2lc40613f

surface, performances of planar PhC-OFMs are often limited by the inefficient "flow-over" technique employed for analyte/fluid transport, instead of PhC intrinsic detection capabilities. On the one hand, the microfluidic system is often unable to selectively deliver analytes where light–matter interaction is strongest, thus limiting sensitivity values. On the other hand, the microfluidic system is ineffective at transporting a large number of molecules to the PhC sensing surface due to slow diffusion kinetic processes, which at low concentrations causes impractically long detection times, thereby increasing the limit of detection values.

Very recently, besides planar PhC structures, vertical PhC structures with high aspect-ratio (greater than 1) obtained by periodic arrangement of air voids in semiconductor or dielectric materials, *e.g.* silicon or silicon dioxide, have been proposed for the fabrication of a second generation of PhC-OFMs, in which the "flow-over" technique is replaced with a "flow-through" strategy, throughout the PhC structure-itself, that exploits air voids as micro/nano-channels for fluid flow.[18–20] The flow-through strategy allows excellent sensitivity and limit of detection to be achieved, while simultaneously reducing detection times with respect to the flow-over technique, both for biological and chemical analyses.[21,22] Mass transport is almost entirely convective rather than diffusive, which provides a stronger signal in significantly less time than the conventional flow-over approach, for both surface and bulk refractive index detection. As for surface refractive index detection, the surface-to-volume ratio is largely increased thus enabling adsorption/binding of a larger number of molecules on the PhC surface. For bulk refractive index detection, light–matter interaction is moved from surface to bulk, thus enabling deeper interaction between light and fluid. Reflection from multiple periodic surfaces instead of reflection from a single surface, as usually happens in planar PhC structures, allows higher signal-to-noise ratios to be achieved both for surface and bulk refractive index detection. Furthermore, such a second generation of PhC-OFMs features fluidic and optical paths that are inherently independent, the former being through the air voids and the latter perpendicular to the air voids. This enables the integration of both fluidic and optical sections on the same chip as the PhC transducer, which is straightforward for 1DPhCs, thus envisioning a novel generation of optical lab-on-chip with advanced on-chip fluidics (sample preparation, liquid mixing, *etc.*) and optical (signal routing and elaboration, signal multiplexing, *etc.*) features.

An analysis of the literature of high aspect-ratio (HAR) PhCs for optofluidic applications points out that the second generation of PhC-OFMs is very promising for both biological and chemical applications, though still in its infancy. A few interesting cases of vertical HAR-1DPhC structures integrated into optofluidic microsystems by using dry etching technology, namely deep reactive ion etching (DRIE),[18,19] or wet etching technology,[20] have been reported in the literature so far. Nunes *et al.*[18] reported the integration of vertical silicon dioxide/air 1DPhCs with an aspect ratio (AR) of about 3, fabricated by trenching a 9 μm-thick silicon dioxide layer, together with microfluidic channels and waveguides on the same chip. A best sensitivity value of 836 nm/RIU (Refractive Index Unit) at 1.55 μm and limit of detection of 6×10^{-5} RIU are claimed for such a microsystem,[23] the former being comparable to sensitivities of state-of-the-art planar PhC structures.[16] St-Gelais *et al.*[19] reported the integration of vertical Fabry-Perot cavities that exploit silicon/air 1DPhC micromirrors with an AR of about 35, together with microfluidic channels and fiber grooves on the same silicon die. A sensitivity value of 907 nm/RIU at 1.55 μm and a resolution of 1.7×10^{-5} RIU are obtained, the latter claimed by authors to be the highest reported for volume refractive index sensors integrated with microfluidic channels.[24] Barillaro *et al.*[20] reported vertical HAR-1DPhC micromirrors integrated into optofluidic microsystems by using silicon wet etching technology. The 1DPhC micromirrors, with an AR of about 40, were fabricated by electrochemical micromachining (ECM) of silicon and integrated on the same chip together with fluidic microchannels obtained by potassium hydroxide (KOH) etching. A sensitivity value of 1049 nm/RIU at 1.55 μm, which is comparable to sensitivities of state-of-the-art integrated refractive index sensors, and limit of detection of 10^{-3} RIU are obtained.[25]

The fabrication of optofluidic microsystems exploiting HAR-PhCs is undoubtedly more challenging than that of optofluidic microsystems exploiting planar PhCs, the former requiring the use of advanced microstructuring technologies that allow in-plane silicon dissolution to be finely controlled both over small (*e.g.* a few micrometers) and large (*e.g.* thousands of micrometers) areas, up to tens of microns in the out-of-plane direction (as opposed to a few tens nanometers of planar PhC-OFMs). Dry etching technologies, *e.g.* DRIE, allow high flexibility in microfabrication with respect to wet etching technology, at higher cost, though they are affected by drawbacks in the out-of-plane direction (*e.g.* limited aspect-ratio, deviation from the verticality, lag-etching of small and large areas, scalloping of etched surfaces, *etc.*[26]) that reduce the optical quality of fabricated photonic structures.[27] Wet etching technologies, *e.g.* KOH-based, allow vertical silicon microstructures with excellent surface flatness to be fabricated on (110)-oriented substrates,[28] at lower cost, though with significantly reduced flexibility and aspect-ratio with respect to dry etching technologies, due to the crystalline-orientation dependent etching rate.[29] In order to enable high flexibility in microfabrication and etching of high quality vertical surfaces, dry (*e.g.* DRIE) and wet (*e.g.* KOH-based) etchings have been combined for the fabrication of optical microsystems for telecommunication applications, in which DRIE-etched microsystems with high aspect-ratio are post-processed by KOH etching to improve the surface quality of optical structures.[30–32] Though significant improvement of the quality of DRIE-etched surfaces has been demonstrated by KOH post-processing (surface roughness reduced up to one order of magnitude), other drawbacks of dry etching technologies in the out-of-plane direction (*e.g.* deviation from verticality, lag-etching problems, *etc.*) are not easily addressable with the same approach. In summary, for the etching of HAR complex microsystems for optofluidic applications, technological problems of dry and wet technologies can be only partially solved by a combination of such technologies. Moreover, such a combination of technologies increases fabrication costs with respect to both dry and wet etching technologies.

More recently, advanced fabrication of complex silicon microstructures (*e.g.* comb-drive actuators, folded springs) and microsystems (*e.g.* MEMS, microgrippers) with sub-micrometer

accuracy at aspect-ratio values well beyond dry etching technologies (about 100) has been proven to be feasible in any research lab by using a wet etching, low cost technology, namely the ECM technology.[33] Though ECM technology has to date been successfully used for the fabrication of vertical (up to 100 μm deep) 1DPhCs with elevated optical quality (*i.e.* deviation from the verticality of about 0.02° and roughness of etched surfaces of about 20 nm for 100 μm-deep structures) at high aspect-ratio values (over 50),[20,34–36] integration of HAR-PhCs on the same chip with microfluidic and optical sections by only using ECM technology has not previously been reported.

In this work, for the first time, we report the demonstration of all-silicon, integrated HAR PhC-OFMs fabricated by ECM technology, which represents a major step towards HAR-PhC optofluidic/biosensing applications, with respect to previous work.[20,34–36] In particular, we detail and discuss design, fabrication, and optofluidic characterization of ECM-fabricated all-silicon HAR PhC-OFMs, in which HAR-1DPhC devices (*i.e.* micromirrors, optical cavities) are integrated, by one-etching-step on the same silicon die, together with microfluidic reservoirs/channels, for the infiltration of liquids in the PhC air gaps, as well as with fiber grooves, for alignment/positioning of readout fibers in front of the PhC for its optical characterization.

Fabrication of PhC-OFMs by ECM technology is performed by exploiting a dynamic control of the etching anisotropy as the electrochemical etching progresses, which allows the silicon dissolution to be switched in real-time from the anisotropic to the isotropic regime. This enables advanced optofluidic microsystem fabrication through the use of functional and sacrificial structures, the former being functional to the microsystem operation and the latter being sacrificed for the accurate microsystem fabrication. Optofluidic characterization of PhC-OFMs, which is performed by both capillary-action and pressure-driven operations, is carried out by measuring the reflectivity spectra of HAR-PhCs upon injection of liquids featuring different refractive index values in the HAR-PhC air gaps, by using readout optical fibers positioned in the on-chip fiber grooves. A best sensitivity value of 670 nm/RIU is achieved, which is comparable to state-of-the-art integrated refractive index sensors, and a limit of detection of about 10^{-3} RIU is obtained, which is limited by the spectral resolution and thermal/amplitude noise of the measurement setup.

Finally, a sandwich assay based on antigen–antibody interactions for the detection of the C-reactive protein (CRP) at a concentration value of 10 mg L^{-1}, which represents the boundary level between physiological and pathological conditions, is successfully carried out, thus providing a proof of concept of the biosensing potential of PhC-OFMs.

This work clearly demonstrates the possibility of using ECM technology for fabricating, at low cost and in any lab, advanced optofluidic microsystems that, upon an exhaustive experimental characterization, show performance comparable with (or higher than) those fabricated with commercial, expensive dry etching technologies (*e.g.* DRIE). This has not previously been reported in the literature and opens new ground in, though not limited to, the optofluidics/biosensing field due to the low-cost and high-flexibility of the ECM technology.

PhC-OFM design and fabrication

PhC-OFMs consist of two main parts: (1) a micromachined silicon substrate, integrating vertical, HAR-1DPhCs operating in the near-infrared region, together with grooves for on-chip positioning/alignment of readout optical fibers in front of the HAR-1DPhC and with reservoirs/microfluidic channels for handling injection of suitable fluids in the HAR-1DPhC air gaps; (2) a glass slab, which is anodically bonded on top of the micromachined silicon substrate, featuring inlet/outlet holes aligned to the reservoirs and equipped with two fitting ports that allow connection of the microsystem with external equipment to be performed for pressure-driven operation. A schematic representation of the PhC-OFM of this work is shown in Fig. 1 (not to scale). Fig. 2(a–d) show scanning electron microscope (SEM) pictures at different magnifications of the micromachined silicon substrate of the PhC-OFM in Fig. 1. The vertical, silicon/air HAR-1DPhC structure is positioned at the intersection between fluidic (through the 1DPhC air gaps) and optical (perpendicular to the 1DPhC air gaps) paths, thus allowing multiple, volume interactions between fluid and light to be exploited within the HAR-1DPhC bulk during optofluidic applications (Fig. 2a). Two large reservoirs in series to the HAR-1DPhC allow injection of fluids in the 1DPhC air gaps to be effectively performed through the fitting ports in the glass cover by pressure-driven operation, as well as by capillary-action upon simply dropping a controlled volume of liquid in one of the reservoirs (Fig. 2a). Fiber grooves (Fig. 2b) allow fine positioning/alignment of readout optical fibers in front of the 1DPhC to be achieved and, in turn, in-plane reflection (and/or transmission) measurements with/without liquids flowing in the HAR-1DPhC to be accomplished with high repeatability/accuracy. The

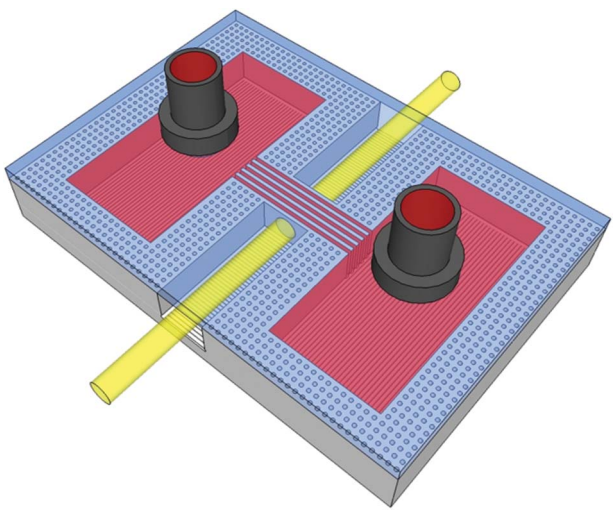

Fig. 1 Schematic representation of the PhC-OFM of this work (not to scale) consisting of two main parts: (1) a micromachined silicon substrate, integrating vertical, HAR-1DPhCs operating in the near-infrared region, grooves for on-chip positioning/alignment of readout optical fibers in front of the HAR-1DPhC, and reservoirs/microfluidic channels for handling injection of suitable fluids in the HAR-1DPhC air gaps; (2) a glass slab which is anodically bonded on top of the micromachined silicon substrate, featuring inlet/outlet holes and equipped with two fitting ports that allow connection of the microsystem with the macroworld.

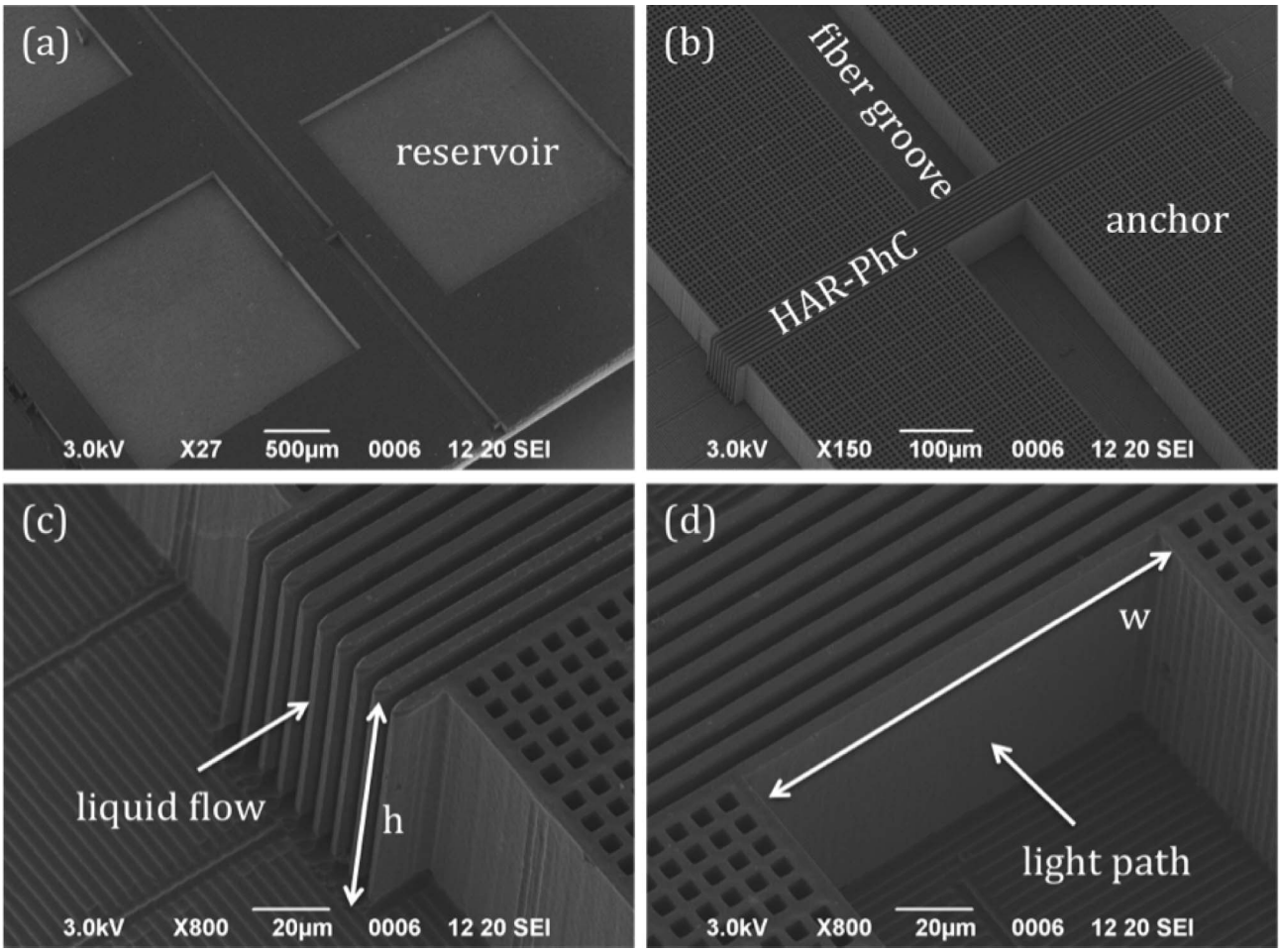

Fig. 2 SEM pictures at different magnifications of the micromachined silicon substrate of the PhC-OFM of Fig. 1, which is fabricated by exploiting advanced features of the ECM technology. (a) Birds-eye view of the whole PhC-OFM. The two large reservoirs in series to the 1DPhC are clearly visible. (b) Magnification of (a) showing the core of the PhC-OFM. The PhC structure is clearly visible at the intersection of optical and fluidic paths. Fiber grooves and anchor structure are also highlighted. (c) Magnification of (b) showing the fluidic inlet section of the HAR-1DPhC. (d) Magnification of (b) highlighting the microstructure of the HAR-1DPhC.

anchor structure (Fig. 2a and 2b) allows mechanical stability of the PhC-OFM to be ensured, as well as leakage of liquid into the fiber grooves during optofluidic operation of the microsystem to be avoided. Details of both the microfluidic inlet section of the 1DPhC and 1DPhC three-dimensional microstructure are shown in Fig. 2c and 2d, respectively, which emphasize the high accuracy in microfabrication of complex microsystems featuring HAR structures, as well as the high quality of surfaces that are achievable by means of the ECM technology used for OFM fabrication.

The core element of the proposed PhC-OFM is a vertical, silicon/air HAR-1DPhC micromirror featuring a number of high-order bandgaps with high-reflectivity in the near-infrared region (1.0–1.7 µm), among which one centered around the operation wavelength λ = 1.55 µm. Design of the 1DPhC micromirror is analytically performed according to the so-called hybrid quarter-wavelength stack,[37] which consists of an array of silicon layers with thickness d_{Si} and air gaps of width d_{Air}, satisfying the conditions $d_{Si} = M\lambda/4n_{Si}$ and $d_{Air} = N\lambda/4$, where M and N are odd integers, independent parameters, n_{Si} is the silicon refractive index at λ (whereas air refractive index is 1), and $n = (M + N)/2$ is the order of the n-th bandgap, which is centred at λ. Design parameters at the operation wavelength λ = 1.55 µm are the silicon refractive index n_{Si} = 3.48, the spatial period $p = d_{Si} + d_{Air}$ = 8 µm, and the porosity of the structure $D = d_{Air}/p$ = 0.62, which gives rise to silicon walls with thickness d_{Si} = 3.04 µm (M = 27) and air gaps with width d_{Air} = 4.96 µm (N = 13) and, in turn, to a high-order bandgap (namely the 20th) centred at λ = 1.55 µm. Both period p and porosity D, and, in turn, the thickness of silicon layers d_{Si} are chosen to obtain a mechanically robust silicon/air HAR-1DPhC able to withstand liquid insertion/extraction in/from the air gaps during optofluidic applications, particularly for capillary-action operation which is performed on the silicon microsystem without a cover on top. Height h and width w of the 1DPhC active section and, in turn, of the fiber grooves, are set to 100 µm and 130 µm, respectively, in order to comply with the diameter of readout optical fibers. The height h of the 1DPhC also defines the height of any other structure etched on the same silicon chip. The size of the reservoirs is set to about 2000 µm × 2000 µm in order to comply with the fitting ports internal/external diameter, which is 1.2/1.5 mm in this work.

Fabrication of PhC-OFMs by ECM technology is performed according to the main technological steps sketched in Fig. 3, which specifically refer to the microsystem of Fig. 1 and 2. The starting material is n-type silicon, orientation (100), with a thin silicon dioxide layer on top. The pattern of the microsystem to be fabricated is defined on a photoresist layer by standard lithography, transferred to the silicon dioxide layer by buffered HF (BHF) etching through the photoresist mask, replicated (seed point formation) into the silicon surface by potassium hydroxide (KOH) etching through the oxide mask (Fig. 3a), and finally grooved into the bulk material by back-side illumination electrochemical etching (BIEE). The BIEE consists of a single-etching-step with an initial anisotropic phase (Fig. 3b), used to etch the seed pattern deep in the substrate and create high aspect-ratio microstructures, and a final isotropic phase (Fig. 3c), used to release sacrificial structures from the substrate while leaving functional structures anchored to it. Two through holes are drilled in a borosilicate glass slab, which is placed on top of the micromachined silicon substrate by anodic bonding and provided with fitting ports for connection of the PhC-OFM with peripheral equipment during pressure-driven optofluidic operation (Fig. 3d). Fig. 4 shows optical microscope pictures of the PhC-OFM of Fig. 2 at different magnifications (Fig. 4a–4c); in Fig. 4d the PhC-OFM is shown with a standard readout optical fiber positioned in the left hand-side groove.

The key role of the PhC-OFM fabrication by ECM technology is played by the back-side illumination electrochemical etching of n-type silicon in HF-aqueous electrolytes,[38] which allows silicon dissolution to be finely controlled in the X–Y plane at the sub-micrometer scale up to hundreds of microns in the Z-direction, thus enabling fabrication of complex microsystems with very high aspect-ratio.[33] BIEE makes use of n-type substrates and back-side illumination to enable silicon dissolution in

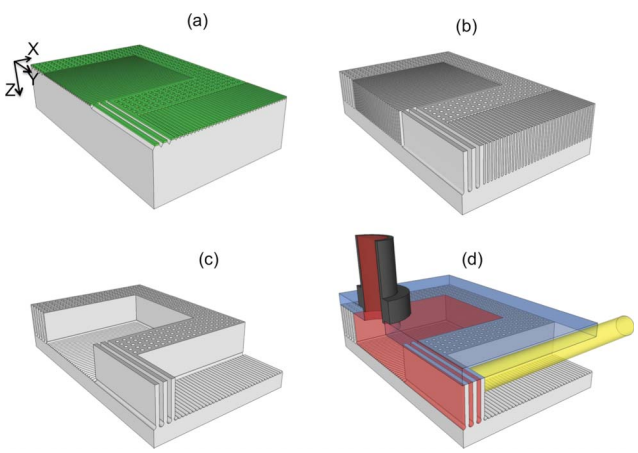

Fig. 3 Main technological steps for the fabrication of PhC-OFMs by ECM technology, with specific reference to the PhC-OFM of Fig. 1 and 2: (a) pattern definition by standard lithography and seed pattern formation on the silicon surface by KOH etching; (b) deep anisotropic etching of the seed pattern by BIEE and fabrication of high aspect-ratio microstructures; (c) isotropic etching of the bottom of the fabricated high aspect-ratio microstructures by BIEE and release of part of the etched microstructures from the substrate; (d) anodic bonding of a borosilicate glass slab, provided with fitting ports, on top of the micromachined silicon substrate.

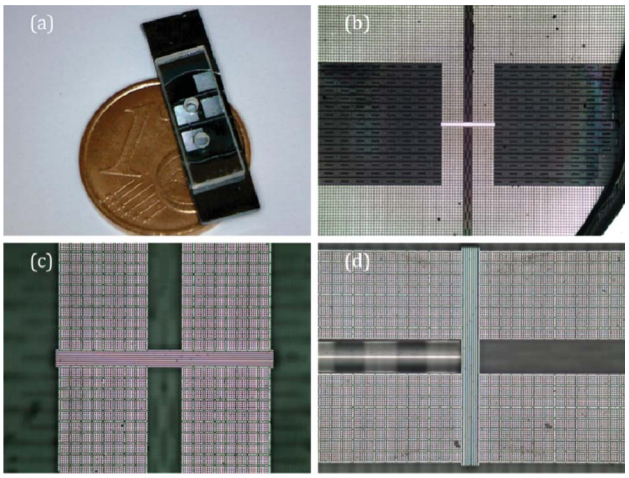

Fig. 4 Optical microscope pictures of the PhC-OFM of Fig. 2 at different magnifications. (a) A silicon chip integrating two PhC-OFMs, featuring a glass cover anodically bonded on its top, is compared to a coin. (b) Top view of one of the PhC-OFMs of (a). (c) Magnification of the core of the PhC-OFM of (b). (d) Magnification of the core of the PhC-OFM with a standard 125 μm-diameter optical fiber positioned in the fiber groove, on left hand side.

HF-aqueous electrolytes, which is hole-activated process under anodic polarization of silicon, only where seed points on the silicon surface were defined by KOH replication of the layout pattern. Sub-micrometric control of silicon dissolution at the seed sites, in the X–Y plane and along the Z-direction, is obtained by properly controlling both the etching current density J_{etch} and the etching voltage V_{etch} as the etch progresses.[33] Details are provided in the Materials and Methods section.

As schematically depicted in Fig. 3, ECM makes use of both functional and sacrificial structures for fabrication of advanced silicon microsystems.[33] Functional structures are, by definition, parts of the microsystem that are anchored (partially, at least) to the silicon substrate after the isotropic phase of the electrochemical etching step. Sacrificial structures are, by definition, parts that are not anchored to the silicon substrate after the isotropic phase of the electrochemical etching step and are hence removed. The former are indeed functional to the microsystem operation, while the latter are sacrificed for the accurate microsystem fabrication. All the microsystem parts visible in the SEM pictures of Fig. 2 are functional structures that were properly designed to withstand the isotropic phase of the etching and are still connected to the substrate at either their bottom or through suitable anchor structures; sacrificial structures in Fig. 2 are no more visible as they were designed to be effectively removed during the isotropic phase of the electrochemical etching step in order to produce fiber grooves as well as reservoirs. Fig. 2c and 2d clearly show the effect of the isotropic phase of the electrochemical etching step on both functional and sacrificial structures: the HAR-1DPhC is anchored to the silicon substrate after the isotropic phase, while sacrificial structures around 1DPhC and anchor structures are removed after the isotropic phase leaving a characteristic ripple on the bottom surface. The use of sacrificial structures allows the simultaneous etching of both small (feature of a few microns) and large (length of several millimeters) areas to be performed at the same rate and

with the same accuracy, thus eliminating lag-effect problems on silicon areas with different aspect-ratios, which is a major problem of dry etching technologies. In addition, fabrication of structures featuring a reduced aspect-ratio value, such as reservoirs, fluidic microchannels, and fiber grooves, is carried out with the same accuracy of structures featuring a high aspect-ratio value, such as 1DPhC and anchor structures, by just exploiting one-etching-step.

Although the fabrication process is here detailed for the specific case of the PhC-OFM of Fig. 1 and 2, optofluidic microsystems differing for both fluidic and optical sections can be effectively produced by using the ECM technology, after a proper design of the microsystem layout has been defined. Fig. 5 shows SEM pictures of the core of four PhC-OFMs differing for a few details concerning both fluidic and optical sections. In Fig. 5a, the PhC-OFM exploits a HAR-PhC with period of 8 μm, height of 100 μm, and width of 300 μm; the HAR-PhC is connected to the reservoirs through two microchannels with length of 250 μm and width of 60 μm and is addressable by means of optical fibers to be positioned in grooves with width of 300 μm. In Fig. 5b and 5c, the two PhC-OFMs exploit HAR-PhCs featuring different periods, 8 μm and 10 μm respectively, and the same height and active width of 100 μm and 130 μm, respectively. In both cases the HAR-PhC directly enter the reservoirs without the need of further fluidic connections and is addressable by means of optical fibers to be positioned in grooves with width of 130 μm. In Fig. 5d, the PhC-OFM exploits a 1DPhC resonant cavity as the core element, which consists of two hybrid quarter-wavelength 1DPhC micromirrors with spatial period of 8 μm separated by a half-wavelength air gap with width of 8 μm; the half-wavelength air gap is connected through microchannels with length of 250 μm to the reservoirs so that it can be filled with proper liquids in order to modulate the wavelength position of the resonance peak of the cavity, and the resonant cavity is addressable by means of optical fibers to be positioned in grooves with width of 300 μm. Insets in Fig. 5a–d show details of the fluidic inlet section of the PhC optical components.

PhC-OFM operation and characterization

Optofluidic characterization of PhC-OFMs is carried out by injecting liquids (water, ethanol, isopropanol, and water/ethanol

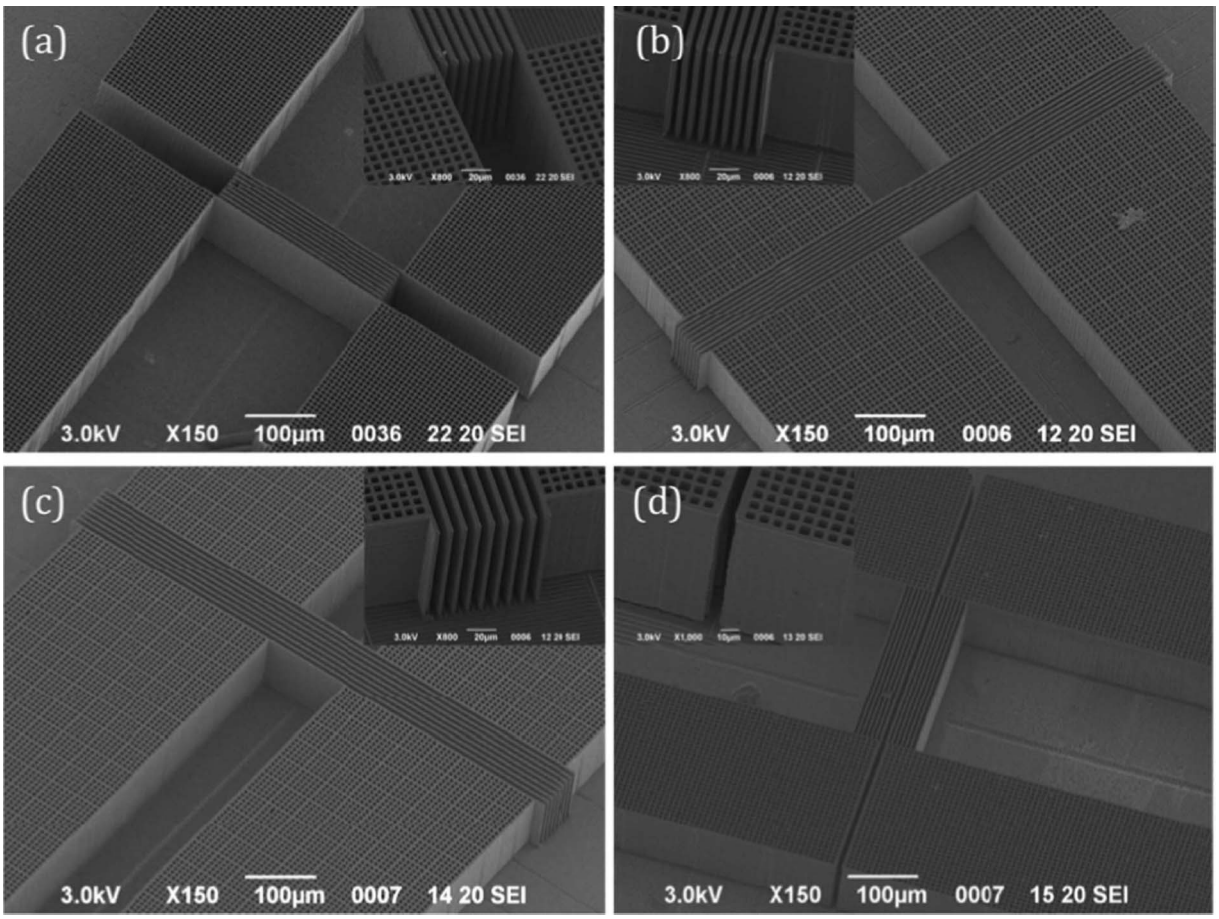

Fig. 5 SEM pictures of the core of four PhC-OFMs differing for a few details concerning both fluidic and optical sections, fabricated by ECM technology. (a) The PhC-OFM exploits a HAR-PhC with period of 8 μm, height of 90 μm, and width of 300 μm; the HAR-PhC is connected to the reservoirs through two microchannels with length of 250 μm and width of 60 μm; the width of the fiber grooves is 300 μm. (b) and (c) The two PhC-OFMs exploit HAR-PhCs with different periods, 8 μm and 10 μm respectively, and same height and width, 90 μm and 130 μm respectively. In both cases the HAR-PhC directly enter the reservoirs; the width of fiber grooves is 130 μm. (d) The PhC-OFM exploits a 1D-PhC resonant cavity as core element; the half-wavelength air gap of the resonant cavity has width of 8 μm and is connected through microchannels with length of 250 μm to the reservoirs; the width of fiber grooves is 300 μm. Insets in Fig. 5a–d show details of the fluidic inlet section of the PhC optical components.

mixtures[39]) with different refractive index values in the HAR-PhC air gaps by both capillary-action and pressure-driven operations. Experimental measurement of the optical power reflected from HAR-PhCs upon liquid injection is performed using optical fibers positioned into the fiber groove in front of the PhC-itself (see Fig. 4d). For each tested liquid, measurement of the reflected power spectrum is performed before infiltration of the PhC with the liquid (empty microsystem), after infiltration of the liquid in the air gaps of the PhC (filled microsystem), and after removal of the liquid from the PhC air gaps (empty microsystem). The procedure is repeated several times for each tested liquid so as to investigate both repeatability and accuracy of the PhC-OFM operation for optofluidic applications. Optical measurements are performed at room temperature, without the use of a feedback loop for temperature monitoring/control. After acquisition, reflected power spectra are normalized with respect to an ideal reflector by numerical elaboration, using the glass–air interface at the output connector as a reference.[35] Experimental reflectivity spectra are low-pass filtered in the Fourier Transform domain in order to increase the signal-to-noise ratio and, in turn, to reduce the effect of measurement noise on the reflectivity peak position. The position of the different reflectivity peaks is then automatically detected.

Capillary-action operation. Capillary-action operation is investigated using three different liquids, namely water, ethanol, and isopropanol, which readily infiltrate the HAR-PhC air gaps by capillary action after a calibrated volume (0.5 μl) of the liquid substance is dropped into one of the reservoirs of the silicon microsystem, in this case without any cover on top. The liquid quickly expands from the reservoir to the PhC structure, uniformly filling the air gaps and producing a dramatic change in the reflectivity spectrum of the HAR-PhC with respect to the reference spectrum in air. The remarkable change in the line-shape of the reflectivity spectrum of the PhC structure is due to the significant increase of the effective refractive index of the photonic material upon replacement of air with liquids, which gives rise to higher order bandgaps to appear in the wavelength range under observation (compare Fig. 6a to Fig. 6b–6d). The change in the line-shape does not significantly depend on the specific liquid infiltrated in the HAR-PhC, as the relatively small variation of the refractive index between the different liquids investigated in this work does not produce any further change in the order of bandgaps in the wavelength range under observation. However, the slight increase of the refractive index value from water to ethanol and isopropanol produces a reliable shift of the reflectivity spectrum toward longer wavelengths.[40] The magnitude of the shift correlates well with the refractive index value of the substance infiltrated in the PhC structure. After the gaps are filled, the liquid starts evaporating from the PhC air gaps with a characteristic time that reduces as the surface tension of the liquid decreases (from water, to ethanol, and isopropanol), thus rapidly bringing the reflectivity spectrum back to the reference spectrum in air.

Typical experimental reflectivity spectra acquired on a PhC-OFM of the type of Fig. 5a both in air (empty microsystem) and after capillary infiltration of the HAR-PhC air gaps with water, ethanol, and isopropanol (filled microsystem) are reported in Fig. 6, along with theoretical reflectivity spectra numerically

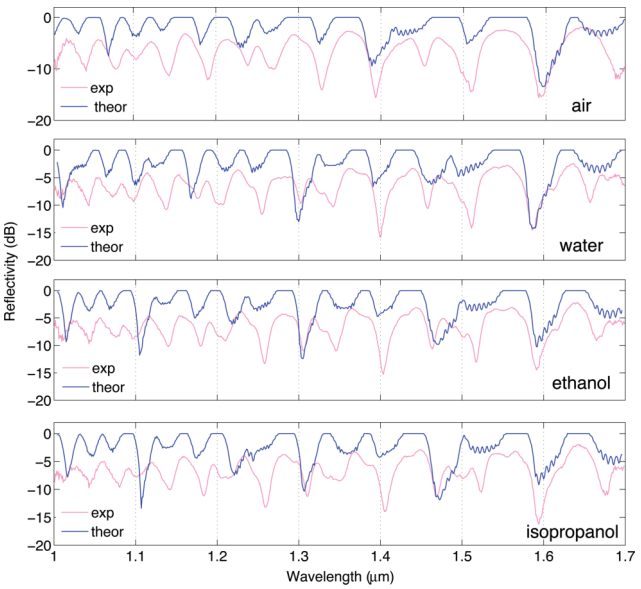

Fig. 6 Typical experimental reflectivity spectra (gray line, pink online) acquired on a PhC-OFM of the type of Fig. 5(a) in air (empty microsystem) and after capillary infiltration of the HAR-PhC air gaps with water, ethanol, and isopropanol (filled microsystem). Theoretical reflectivity spectra (black line, blue online) numerically calculated by using the characteristic matrix method through best fitting of the experimental data (D = 0.624, σ_D = 5 × 10^{-4}, RB = 10 nm, and SD = 5 μm) are also reported.

calculated by using the characteristic matrix method, which was properly modified to take into account both non-idealities of the 1DPhC (*i.e.* roughness in the Y–Z plane, silicon/air thickness variation in the X direction) and limitations of the measuring setup (*i.e.* resolution bandwidth, RB, of the optical spectrum analyzer; spot diameter, SD, of the interrogating beam).[35] Good agreement between experimental and theoretical reflectivity spectra is observed for air as well as for the three tested liquids, though theoretical flat bandgap plateaux appear as experimental broad high-reflectivity peaks due to scattering effects (not taken into account in this work) at the Y–Z silicon surface of PhCs. Theoretical spectra in Fig. 6 are calculated through best-fitting of the experimental data, using porosity mean value D and standard deviation σ_D as fitting parameters, under the hypothesis that porosity follows a Gaussian statistical distribution; the limited resolution bandwidth, RB = 10 nm, and the beam spot-size, SD = 5 μm, employed for the measurement are also taken into account. The mean value D basically sets the spectral position of reflectivity bandgaps (high-reflectivity regions), and the standard deviation value σ_D essentially settles the extinction ratio between high- and low-reflectivity regions.[35] According to porosity definition, the mean value D can be directly translated into silicon thickness, $d_{Si} = p(1-D)$. On the other hand, the porosity standard deviation σ_D can be related to the peak-to-valley amplitude of the surface roughness $\rho = p3\sigma_D$, with probability 0.997. The fitting procedure yields D = 0.624 and σ_D = 5 × 10^{-4} (ρ = 12 nm) for the experimental reflectivity spectra of Fig. 6, which is in good agreement with SEM observation of PhC micromachined surfaces and confirm the good optical quality of PhC fabricated by ECM technology.

Fig. 7a (right axis) shows mean value (symbols) and standard deviation (error bars) of the position of reflectivity peaks of experimental spectra acquired on a PhC-OFM of the type of Fig. 5a (the same device of Fig. 6) upon capillary infiltration of the microsystem with water, ethanol, and isopropanol. Recorded spectra highlight that good repeatability is achieved both in air as well as with the liquid infiltrating the PhC structure (see Fig. S1a, ESI†), as it can be argued by standard deviation values of peak positions reported in Fig. 7. A good linear relationship is observed for any of the reflectivity peaks as a function of the refractive index value of the liquids infiltrating the air gaps, as can be observed in Fig. 7b and 7c for the peaks at 1.55 μm and 1.63 μm, respectively. A maximum standard deviation value of about 1 nm is obtained over the whole set of peaks. Fig. 7a (left axis) also shows theoretical bandgap regions (green areas) of the same 1DPhC in the wavelength interval under observation, from 1 μm up to 1.7 μm, as a function of the refractive index value of the medium filling the PhC air gaps, from 1.32 RIU up to 1.37 RIU. Bandgap regions are defined as wavelength intervals featuring a reflectivity value

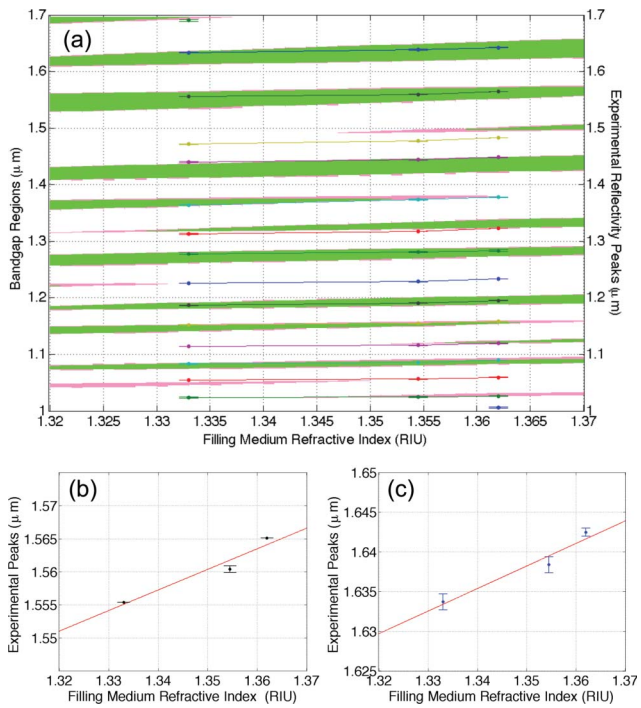

Fig. 7 (a) (Right axis) Mean value (symbols) and standard deviation (error bars) of the position of reflectivity peaks of experimental spectra acquired on a PhC-OFM of the type of Fig. 5(a) upon capillary-action infiltration of the microsystem with water, ethanol, and isopropanol. (Left axis) Theoretical bandgap regions (reflectivity > 0.999) and high-reflectivity regions (reflectivity > 0.95) numerically calculated by means of the modified characteristic matrix method above described, using D = 0.624, $\sigma_D = 5 \times 10^{-4}$, RB = 10 nm, and SD = 5 μm as parameters. (b) Mean value (symbols) and standard deviation (error bar) of the experimental reflectivity peak falling within the bandgaps at 1.55 μm (in water) as a function of the refractive index value of the liquid filling the air gaps. (c) Mean value (symbols) and standard deviation (error bar) of the experimental reflectivity peak falling within the bandgaps at 1.63 μm (in water) as a function of the refractive index value of the liquid filling the air gaps.

higher than 0.999 and are numerically calculated by means of the modified characteristic matrix method above described, using D = 0.624, $\sigma_D = 5 \times 10^{-4}$, RB = 10 nm, and SD = 5 μm as parameters. High-reflectivity regions (pink areas), which are defined as wavelength intervals with reflectivity higher than 0.95, are also reported in Fig. 7 and include bandgap regions where appropriate. Both position and width of the 1DPhC bandgap regions significantly change with the refractive index value of the medium filling the air gaps, thus theoretically supporting the possibility of using the proposed PhC structures as integrated devices for optofluidic applications, in general, as well as for future label-free sensors, in particular. Experimental data on position and shift of reflectivity peaks as a function of the refractive index of the liquid infiltrating the PhC structure (Fig. 7a) agree well with theoretical predictions of bandgap regions, apart from a few experimental reflectivity peaks that do not fall within the theoretical bandgap regions (green areas). The existence of such reflectivity peaks can be interpreted in terms of regions with high reflectivity, though lower than 0.999. Both position and shift of such experimental reflectivity peaks are in good agreement with numerically calculated high reflectivity regions (pink areas), as shown in Fig. 7a.

In view of the application of the proposed PhC-OFMs as integrated refractive index sensors an estimation of both sensitivity (S) and limit of detection (LoD) is performed by analyzing the two experimental reflectivity peaks falling within the bandgaps at 1.55 μm and 1.63 μm (in water), which are the most significant both from research and commercial point of views. By best fitting experimental data with a linear relationship, a sensitivity (defined as wavelength shift as a function of refractive index variation) $S = d\lambda/dn$ = 310 nm/RIU and 280 nm/RIU is obtained for the two peaks, respectively, which are comparable to sensitivity values of refractive index sensors reported in the literature and exploiting photonic crystals. The use of a linear function for the fitting of experimental data is well supported by theoretical predictions, at least in the refractive index range investigated in this work.[20]

An estimation of the actual limit of detection of the proposed PhC-OFM cannot be easily performed due to both the limited spectral resolution (0.8 nm step) and the high value of the OSA resolution bandwidth (10 nm) required for ensuring sufficiently high signal-to-noise ratio and dynamics in the measurements. It is well known that the LoD value can be calculated as LoD = R/S, being R the system resolution that is typically established as 3·STD, with STD standard deviation of the noise in the system. The STD value can be expressed as, $\mathrm{STD} = \sqrt{(\mathrm{STD}^2_{\mathrm{ampl-noise}} + \mathrm{STD}^2_{\mathrm{temp-var}} + \mathrm{STD}^2_{\mathrm{spect-res}})}$, where $\mathrm{STD}_{\mathrm{ampl\text{-}noise}}$ is the variance of the amplitude noise, $\mathrm{STD}_{\mathrm{temp\text{-}var}}$ is the variance of the thermal noise, and $\mathrm{STD}_{\mathrm{spect\text{-}res}}$ is the variance of the quantization error due to spectral resolution limitation. For a fixed spectral resolution (SR) value, the resulting error can be modeled as quantization error, so that the error in determining the position of a reflectivity peak is uniformly distributed between −0.5·SR and + 0.5·SR, and has a resulting standard deviation of 0.29·SR, that is $\mathrm{STD}_{\mathrm{spect\text{-}res}}$ = 0.232 nm in this work. In addition, we expect that a significant contribution to the total STD of the system also comes from thermally-induced variations, being optofluidic measurements performed at room temperature on PhC-OFMs that are not temperature-stabilized, as well as from

amplitude noise sources. A worst-case estimation yields $LoD_{worst} = 3 \cdot STD/S = 4.8 \times 10^{-3}$ RIU and 10.7×10^{-3} RIU for the reflectivity peaks within the bandgap at 1.55 μm and at 1.63 μm (in water), respectively, which are calculated using standard deviation maximum values, STD = 0.5 nm in Fig. 7b and STD = 1 nm in Fig. 7c. Though STD values for LoD_{worst} estimation refer to multiple measurements performed to the PhC-OFM of Fig. 7, measurements performed on a larger set of PhC-OFMs, both under capillary-action and pressure-driven operations, show that STD worst values over different PhC-OFM fabricated by ECM-technology are of the same order of magnitude, that is to say of a few nanometers. It is expected that a significant improvement of the LoD of the system will be achieved by performing temperature stabilization of the OFM as well as by improving both the spectral resolution and the resolution bandwidth, for example reducing the wavelength step, using an amplified spontaneous emission source, and limiting the spectral measurement to a narrow wavelength interval around the bandgap of interest.

Pressure-driven operation. Pressure-driven operation is investigated by injecting water, ethanol, as well as aqueous solutions featuring refractive index values between those of water and ethanol, in the PhC-OFM through the use of a syringe pump at flow rate of the order of 10 μL min^{-1}.

Fig. 8a (right axis) shows mean value (symbols) and standard deviation (error bars) of the position of reflectivity peaks of experimental spectra acquired on a PhC-OFM of the type of Fig. 5(b) under pressure-driven operation, upon infiltration of the microsystem with water, ethanol, and water/ethanol mixtures with different refractive indices. A good linear relationship is observed for any of the reflectivity peaks as a function of the refractive index value of the liquids infiltrating the air gaps. A maximum standard deviation value of about 3 nm is obtained over the whole set of peaks, thus indicating that good repeatability is obtained after cycling the different liquids several times through the microsystem (see Fig. S1b, ESI†). Fig. 8a (left axis) also shows theoretical bandgap regions (green areas) and high-reflectivity regions (pink areas) of the same 1DPhC in the wavelength interval under observation, from 1 μm up to 1.7 μm, as a function of the refractive index value of the medium filling the PhC air gaps, from 1.32 RIU up to 1.37 RIU. Bandgap regions and high-reflectivity regions were numerically calculated by means of the modified characteristic matrix method previously described, using $D = 0.604$, $\sigma_D = 5 \times 10^{-4}$, which are obtained by best fitting experimental reflectivity spectra in the whole wavelength range under observation, with RB = 10 nm and SD = 10 μm. Fig. 8b and 8c show the two experimental reflectivity peaks falling within the bandgaps at 1.5 μm and 1.65 μm (in water), respectively, as a function of the refractive index value of the liquid filling the air gaps. By best fitting experimental data of Fig. 8b and 8c with a linear relationship, a sensitivity $S = d\lambda/dn = 460$ nm/RIU and 670 nm/RIU is obtained for the two peaks, respectively. A worst-case estimation of the limit of detection yields $LoD_{worst} = 3 \cdot STD/S = 17.6 \times 10^{-3}$ RIU and 14.3×10^{-3} RIU for the reflectivity peaks within the bandgap at 1.5 μm and 1.65 μm (in water), respectively, which are calculated using standard deviation maximum values, STD = 2.7 nm in Fig. 8b and STD = 3.2 nm in Fig. 8c, obtained from

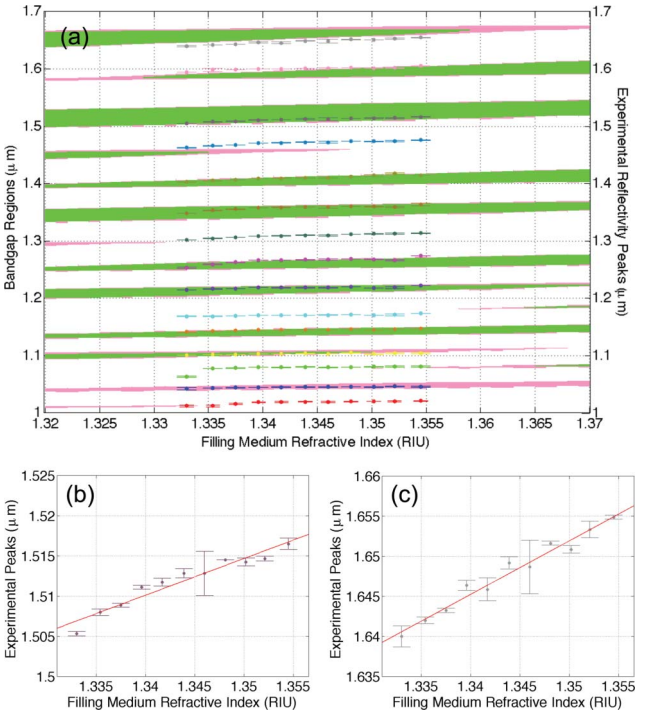

Fig. 8 (a) (Right axis) Mean value (symbols) and standard deviation (error bars) of the position of reflectivity peaks of experimental spectra acquired on a PhC-OFM of the type of Fig. 5(b) under pressure-driven operation, upon infiltration of the microsystem with water, ethanol, and water/ethanol mixed solutions with different refractive indices. (Left axis) Theoretical bandgap regions (reflectivity > 0.999) and high-reflectivity regions (reflectivity > 0.95) numerically calculated by means of the modified characteristic matrix method above described, using $D = 0.604$, $\sigma_D = 5 \times 10^{-4}$, RB = 10 nm, and SD = 10 μm as parameters. (b) Mean value (symbols) and standard deviation (error bar) of the experimental reflectivity peak falling within the bandgaps at 1.5 μm (in water) as a function of the refractive index value of the liquid filling the air gaps. (c) Mean value (symbols) and standard deviation (error bar) of the experimental reflectivity peak falling within the bandgaps at 1.65 μm (in water) as a function of the refractive index value of the liquid filling the air gaps.

experimental spectral measurements. It must be pointed out that besides limitations of the optical setup, which were described in the previous section, LoD values are, in this particular case, affected by the standard deviation of the spectral measurements performed with the solution containing 60% of ethanol in water, which is clearly an outlier in the whole set of measurements, probably due to air bubbles traveling in the 1DPhC during one of the measurement cycles with this specific solution. If we recognize the error bar of the measurement with the mixture containing 60% of ethanol in water as an outlier, we can exclude it from the LoD calculation, thus reducing the LoD value to 4.5×10^{-3} RIU and 5.8×10^{-3} RIU, which are of the same order of magnitude as for capillary-action operation.

Biosensing with PhC-OFMs: proof-of-concept of an immunoassay for CRP. The proof of concept about the biosensing potential of PhC-OFMs is given by succesfully carrying out a sandwich assay based on antigen–antibody interactions for the detection of the C-reactive proteine (CRP), under pressure-driven operation

through the use of a syringe pump at flow rate of the order of 10 μL min^{-1}.

Infection is an important process in all medical disciplines, which may represent a sign of sepsis, one of the most important causes of death. Severe infection and sepsis are a common, expensive, and frequently fatal condition, with as many deaths annually as those from acute myocardial infarction.[42] Even if it was not considered a useful clinical parameter for many years because of its absence of specificity, nowadays CRP is measured as a sensitive systemic marker of inflammation, infection, and tissue damage. Moreover it has recently emerged as an interesting novel and potentially clinically useful marker for increased cardiovascular risk.

The chosen immunoassay is specific for the C-reactive protein, which was the first acute-phase protein to be described in the literature.[43] The CRP concentration value is chosen at the boundary level between physiological and pathological conditions, being the circulating concentration of human CRP increasing from normal levels of about 1–10 mg L^{-1} up to either 20–40 mg L^{-1} for viral infection or about 500 mg L^{-1} in case of bacterial infection. Clone C5 and clone C6 are used as capture and detection specific antibody, respectively, for CRP.

At first, carbonate buffer (10 mM CH_3COONa, pH 5.5) is pumped for 30 min throughout the PhC-OFM in order to prepare PhC surfaces for the capture-antibody deposition step (*step 1*). Clone C5 capture-antibody in carbonate buffer (10 mg L^{-1} clone C5) is let deposit into the PhC surfaces for 60 min, then the PhC-OFM is rinsed with carbonate buffer. In order to optimize interaction conditions between CRP and antibody,[44] the PhC-OFM is rinsed for 30 min with HEPES buffer (10 mM HEPES, 2 mM $CaCl_2$, pH 7.4) (*step 2*). A passivation step of the PhC surfaces is performed using bovine serum albumin (BSA) in HEPES (0.1% BSA) for 15 min, then the PhC-OFM is rinsed with HEPES buffer for 15 min (*step 3*). The antigen in HEPES buffer is let incubate with the capture-antibody for 30 min (10 mg L^{-1} CRP), then the PhC-OFM is rinsed in HEPES buffer for 15 min (*step 4*). Clone C6 detection-antibody in HEPES buffer is let incubate for 30 min (10 mg L^{-1} clone C6). A rinsing step of the PhC-OFM with HEPES buffer for 15 min is eventually performed (*step 5*).

Fig. 9a shows mean value (symbols) and standard deviation (error bars) of the position of reflectivity peaks of experimental spectra acquired on a PhC-OFM of the type of Fig. 5(b), under pressure-driven operation, after the main chemical steps of the sandwich assay above described. Typical standard deviation values around 1 nm are obtained over the whole set of peaks, thus indicating that the sandwich assay is fully carried out with good repeatability on the PhC-OFM. Fig. 9b and 9c show details of the wavelength position of the experimental reflectivity peaks at 1.53 μm and 1.63 μm, respectively, after the main chemical steps. A monotonic red shift of the peak position is obtained after each chemical step (*steps* 1–5) for the whole set of peaks, as it is clear from Fig. 9a and 9b, thus well demonstrating that adsorption of biological materials on the PhC surfaces, in general, as well as antigen–antibody interaction at the PhC surfaces, in particular, are successfully monitored through the use of the PhC-OFM. In fact, as all the measurements were performed in the same buffer solution (apart from *step* 1), the experimental shift of the wavelength position of reflectivity peaks

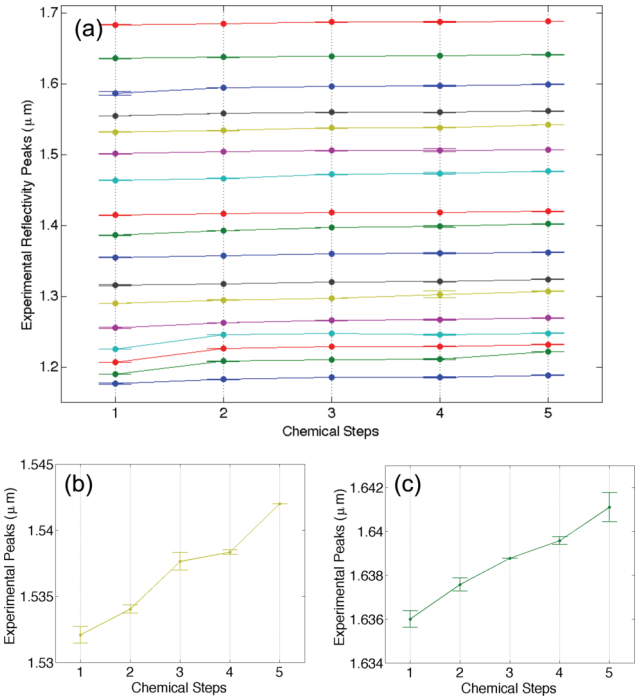

Fig. 9 (a) Mean value (symbols) and standard deviation (error bars) of the position of reflectivity peaks of experimental spectra acquired on a PhC-OFM of the type of Fig. 5(b) under pressure-driven operation, in carbonate buffer before capture-antibody deposition (*step* 1), in HEPES buffer after capture-antibody deposition (*step* 2), in HEPES buffer after BSA passivation (*step* 3), in HEPES buffer after antigen incubation (*step* 4), in HEPES buffer after detection-antibody incubation (*step* 5). (b) Mean value (symbols) and standard deviation (error bar) of the experimental reflectivity peak at 1.53 μm as a function of the chemical *steps*. (c) Mean value (symbols) and standard deviation (error bar) of the experimental reflectivity peak at 1.63 μm as a function of the chemical *steps*.

is directly related to adsorption and/or interaction processes occurring at the PhC surfaces, whose effect is amplified by multiple reflections within the photonic crystal transducer.

Materials and methods

PhC-OFM design

Design rules. The layout design of PhC-OFMs fabricated by ECM technology was carried out according to the following main rules: 1) porosity of functional structures, that is silicon areas patterned with anchor structures and photonic crystal structures, was set by design to a value of 23% for the former and 50% for the latter; 2) after functional structures were properly designed, the remaining silicon area was partitioned with sacrificial structures with a porosity value of 50% by design; 3) two layout elements were separated by a distance with minimum dimension of 2 μm and maximum dimension of 4 μm; 4) each layout element had by design a width ranging between a minimum dimension of 2 μm and a maximum dimension of 6 μm; 5) anchor structures were designed to enclose parts sufficiently larger than sacrificial structures, in order to effectively withstand the isotropic phase of the electrochemical etching step; 6) sacrificial structures consisted of basic elements

(*i.e.*, a straight line with proper length and width), designed to become free-standing during the isotropic phase of the electrochemical etching, which were arranged as one-dimensional array of parallel lines, with number of elements and array orientation chosen to comply with issues 2) and 3).

For the sake of clarity, the design values of structural and sacrificial structures used for the fabrication of the microsystem in Fig. 2 are provided below. Anchor structures consisted of a two-dimensional repetition of a 5 × 5 square lattice of holes with side of 4 μm and pitch of 8 μm enclosed by a silicon frame with width of 6 μm; photonic crystals consisted of one-dimensional array of 850 μm-long parallel lines with a width of 4 μm and a pitch of 8 μm; basic elements of sacrificial structures consisted of straight lines with width of 2 μm and pitch of 4 μm.

PhC-OFM fabrication

Silicon wafers. All the experiments were carried out on (100) n-type CZ-grown silicon substrates, provided by STMicroelectronics, with resistivity 2.5–8.5 Ω ·cm. A 200-nm-thick silicon dioxide layer was grown by dry thermal oxidation in pure O_2 atmosphere at 1050 °C for 4 h, in a ThermoLyne 21100 tube furnace.

Pattern definition. A Microposit S-1818 photoresist (from Shipley) film was deposited on the silicon wafer by spin-coating at 4000 rpm for 60 s and subsequent soft-baking on a hot-plate at 115 °C for 90 s. UV contact lithography system (MJB3 Karl-Suss mask aligner) was used for layout pattern definition. Photoresist development and post-backing were carried out by using 1 : 5 (by volume) Microposit developer 351:H_2O solution and hot-plate at 115 °C for 90 s, respectively. Once the lithographic step was ended, the layout pattern was transferred to the silicon dioxide layer by wet etching in a 6% wt. buffered HF (BHF) solution for 120 s.

KOH etching. The pattern was transferred to the silicon substrate by wet etching in a 25 wt% KOH solution, saturated with isopropanol to improve the etching uniformity, at 50 °C. The etching time was chosen long enough to obtain formation of full-V grooves for all patterned geometries. The silicon dioxide layer, which was used as masking layer during the alkaline etching, was removed after that by wet etch in a 1 : 1 (by volume) HF (48%):ethanol (99.9%) solution.

Back-side illumination electrochemical etching (BIEE). The experimental setup used for the electrochemical etching consisted of a PTFE (polytetrafluoroetylene) electrochemical cell having a volume of 400 cm^3. The front side of the silicon sample was in contact with the solution. The area of the sample exposed to the electrolyte was about 0.66 cm^2 and had a circular shape. The electrolyte composition was 5 vol% HF : 95 vol% H_2O, with 1000 ppm of sodium lauryl sulfate (SLS) as wetting agent. The surfactant was added to reduce the formation of hydrogen bubbles at the sample surface, thus enhancing the etching uniformity. For the same reason, the solution was stirred during the anodization process. Back side illumination of the sample was performed with a 250 W halogen lamp, positioned about 3.5 cm apart from the sample, through a circular window (0.66 cm^2) in the metal electrode used to provide the electrical contact to the sample. A feedback loop, performed by using a PID controller (Eurotherm 2604), allowed the lamp power, and thus the illumination intensity, to be changed in order to proper set the etching current density value as the etching progressed. An IR filter with a cutoff wavelength of 750 nm was placed between the lamp and the silicon sample in order to avoid carrier generation close to the silicon surface in contact with the electrolyte. A second feedback loop, also obtained with the same PID controller, allowed the working temperature to be maintained at 22 °C for the entire etching time. The cathode consisted of a platinum disc in front of the silicon anode at a distance of 1 cm, whereas a platinum wire close to the silicon electrode, at a distance of about 2 mm, is used as a pseudo-reference electrode. A Source Measure Unit (Keithley 2410 Source Meter) was used to apply the anodization voltage, between the silicon sample and the reference electrode, and to monitor the etching current.

J–V curves required to obtain the ECM working region, $J_{etch}<J_{peak}$ and $V_{etch}>V_{peak}$ (Fig. S2, ESI†), of the electrochemical system under investigation were recorded under back-side high-intensity illumination of the silicon electrode, by driving the halogen lamp at its maximum power value (250 W). The electropolishing etching current density and voltage values were J_{peak} = 64.79 mA cm^{-2} and V_{peak} = 0.8 V.

As for the anisotropic phase, the etching voltage V_{etch} was set to a constant value of 3 V for the entire etching process, while the etching current density is set to an initial value J_{etch0} = 35.17 mA cm^{-2} and linearly reduced over time with a rate of 2.5 μA cm^{-2} s according to a first-order approximation of the diffusion kinetics of HF molecules from top to bottom of the etched structures, in order to get a constant porosity and, in turn, a perfect anisotropic etching throughout the whole etching depth.[41] Although a better control of the etching process is achieved by modulating the V_{etch} value over time,[33] good results in microfabrication are also obtained using a constant V_{etch} value by only modulating the J_{etch} value over time, as demonstrated in this work for etching depth up to 100 μm (Fig. S1, ESI†). The J_{etch0} value was tailored on the basis of the J_{peak} value in order to obtain a constant porosity mean value of the whole microsystem of 55%, which was experimentally found to give rise to photonic crystal and sacrificial structures with porosity of 62% and anchor structures with porosity of 43%. In fact, experimental observations performed by SEM analysis on a large set of ECM-fabricated complex microsystems containing silicon areas patterned with structures with fairly different geometries such as sacrificial and anchor structures, highlight that though the mean value of the porosity of the whole microsystem is actually set by the J_{etch} value, the specific porosity value of each patterned area significantly depends on the pattern features (*e.g.* layout porosity, pattern geometry, *etc.*) in a non-trivial way. For instance, $P_{avg} = J_{etch}/J_{peak} = V_{etch}/V_{tot} = (P_1 \cdot A_1 + P_2 \cdot A_2)/A_{tot}$ = 0.54 which is close to the expected average value of the microsystem porosity, being P_1 = 0.62 and A_1 = 0.24 cm^2 experimental porosity and area of photonic crystal and sacrificial structures, respectively; P_2 = 0.4218 and A_2 = 0.42 cm^2 experimental porosity and area of anchor structures; A_{tot} = 0.66 cm^2 the whole silicon area subjected to electrochemical etching. The etching time of the anisotropic phase t_{etch} = 3900 s was chosen to fully etch 95 μm-deep trenches.

As for the isotropic phase, after the desired depth was obtained, the value of J_{etch} was abruptly increased from 25.32 mA cm^{-2}, which corresponds to the etching current density value at the end of the anisotropic phase, to 40.32 mA and kept constant for the next 150 s in order to isotropically etch the silicon for a further depth of 5 μm.

Glass slab. A milling machine (CAM-100 VHF) digitally automated *via* computer numerical control (CNC) and equipped with a diamond tip was used to drill two through-holes (1.2 mm diameter), 4 mm far apart, in a borosilicate glass slab (800 μm thick) to be used as a chip cover.

Anodic bonding. The glass cover was anodically bonded to the micromachined silicon substrate using a voltage of 600 V at the temperature of 400 °C. In order to remove organic contaminants off the substrates, the micromachined silicon substrate and glass cover were immersed before bonding in Piranha solution, consisting of 1 : 1 (by volume) H_2SO_4(96%) : H_2O_2(30%), heated at the temperature of 100 °C. The silicon substrate was then rinsed in 1 : 1 (by volume) HF (48%) : ethanol (99.9%) solution for 120 s to remove from the silicon surface thin oxide layer formed during previous cleaning step. After bonding, the microsystem was equipped with two stainless steal fitting ports having internal/external diameter of 1.0/1.2 mm and allowing easy-to-use fluidic connections of the chip to an external setup.

PhC-OFM characterization

Optical measurement setup. Measurements of spectral reflectivity on PhC-OFMs were performed with the optical setup reported in Fig. S3, ESI.† Fiber groove and photonic crystal sensing region were monitored on a computer by placing the PhC-OFM under a microscope connected to a digital CMOS camera. Radiation in the range 1.0–1.7 μm generated by a white lamp was launched toward the PhC by means of a standard telecom SMR-28 (9/125/250 μm core/cladding/coating diameter) fiber-optic 50% coupler, which also carried the reflected light back to the optical spectrum analyzer (OSA). For the measurements on PhC-OFMs without a glass cover, exploiting capillary action, a tapered lensed fiber with standard 125 μm diameter (from OzOptics) was connected to the output port of the coupler and the lensed tip was laid down on the bottom of the groove. A beam spot diameter of 5 μm on the front facet of the PhC was typically obtained. Reflectivity measurements on PhC-OFMs equipped with glass cover, exploiting pressure-driven operation, were performed by using a home-made reduced-diameter (approximately 65–85 μm) fiber tip with a 1° angled termination, which was obtained from a standard 125 μm diameter fiber (SMR-28), positioned in the fiber groove. A beam spot diameter of 10–12 μm on the front facet of the PhC was typically obtained. Fiber positioning in the groove was performed in both cases by means of a manual nanopositioning xyz stage. The fiber-tip/PhC optimal working distance was obtained by maximizing the reflected power in the bandgap wavelength regions, and was of about 26 μm for the lensed fiber and 16 μm for the home-made tip. The 1° angled termination of the home-made reduced tip did not completely eliminate the Fabry-Perot cavity effect between fiber tip and PhC, which was negligible with the lensed termination. On the other hand, the residual ripple on reflectivity spectra with the 1° angled termination did not affect reflectivity peak recognition. A few preliminary experiments were performed on reference PhC samples for directly comparing the results obtained with the lensed-tip and the home-made termination. Apart from the residual ripple, the spectral line shapes were similar, though deeper reflectivity notches could be observed with the lensed fiber due to the smaller spot diameter.[35] Normalization of the reflected power spectra with respect to an ideal reflector was carried out by numerical elaboration using the glass-air interface at the output connector as a reference.[35]

Optical fiber thinning. Home-made fiber tips for pressure-driven characterization of the PhC-OFM were prepared by means of an optical fiber thinning procedure consisting of a HF-based etching step, which was used to reduce the diameter of standard telecom SMR-28 fiber from 125 μm to 65–85 μm. The acrylic coating was mechanically stripped off for a fiber length of 5 cm; this bare-fiber ending section was then cleaned with ethanol and dipped in a HF-based solution at room temperature for 25 min and 30 min in order to reduce the fiber diameter in the range of 80–85 μm and 65–70 μm, respectively. After the thinning procedure, etched fibers were washed in DI water. Optical fibers with 1° angled termination were obtained by cleaving the fiber within the reduced diameter section.

Conclusions

In this work, all-silicon PhC-OFMs of the second generation, in which HAR-1DPhC devices (*i.e.* micromirrors, optical cavities) are integrated on the same silicon die together with microfluidic reservoirs/channels for the infiltration of liquids in the PhC air gaps, and with fiber grooves for alignment/positioning of readout optical fibers in front of the PhC, is for the first time demonstrated to be feasible in any lab at low cost and with high flexibility by using ECM technology.

Fabrication of PhC-OFMs by ECM technology is performed through the exploitation of a dynamic control of the etching anisotropy as the electrochemical etching progresses, which allows the silicon dissolution to be effectively switched in real-time from the anisotropic to the isotropic regime and enables microstructuring of optofluidic systems to be carried out through the use of both functional and sacrificial structures, with submicrometric accuracy at aspect-ratio values not manageable by up-to-date wet and dry microstructuring technologies. In particular, surface quality of ECM-fabricated HAR-PhC structures, with peak-to-valley estimated to be of about ten nanometers and deviation from verticality of about 0.02° up to depth of 100 μm, is superior to that of state-of-the-art DRIE etching technologies at the HR values reached in this work.

Optofluidic characterization of PhC-OFMs is successfully performed by both capillary-action and pressure-driven operations, through measurements of the reflectivity spectra of HAR-PhCs upon injection of liquids featuring different refractive index values in the HAR-PhC air gaps, by using readout optical fibers positioned in the on-chip fiber grooves. High sensitivity and good limit of detection for the PhC-OFMs of this work are obtained for both capillary-action and pressure-driven operations, with a best sensitivity value of 670 nm/RIU, which is

comparable to state-of-the-art integrated refractive index sensors, and a best limit of detection of the order of 10^{-3} RIU, which is significantly limited by constraints of the experimental setup and it is expected to be strongly improved by providing the measurement setup with a temperature control system as well as by recording the reflectivity spectra using a better spectral resolution and smaller resolution bandwidth.

Future biosensing applications are envisaged for the PhC-OFMs of this work. Pressure-driven operation allows PhC-OFMs to be used upon connection with a standard syringe pump (or peristaltic pump), which is mandatory for biosensing applications. In fact, biosensing applications require, for example, an effective immobilization on the PhC surface of suitable biological recognition elements capable of selectively binding specific target analytes. This can be performed *via* pressure-driven flow of proper solutions through the PhC. On the other hand, capillary-action operation opens new exciting possibilities concerning a drop-and-measure approach for such PhC-OFMs, which allows detection of specific analytes to be performed on pre-functionalized OFMs without further connection to fluidic peripheral equipment. The drop-and-measure approach allows the reduction of both volume and waste of biological samples as well as power dissipation and size, while increasing portability and point-of-care operation. Proof of concept of the biosensing potential of PhC-OFMs is given under pressure-driven operation by successfully carrying out a sandwich assay based on antigen–antibody interactions for the detection of the C-reactive protein at a concentration value of 10 mg L^{-1}, which represents the boundary level between physiological and pathological conditions.

Acknowledgements

This work was partially supported by the Ministero dell'Istruzione, dell'Università e della Ricerca (MIUR) Italiana in the framework of the Progetti di Ricerca di Interesse Nazionale (PRIN) 2007. Currently, S. Surdo holds a fellowship funded by Fondazione Alma Mater Ticinensis, Pavia, Italy.

References

1 X. Fan and I. M. White, *Nat. Photonics*, 2011, **5**, 591.
2 Y. Zhao, X. Zhao and Z. Gu, *Adv. Funct. Mater.*, 2010, **20**, 2970.
3 S.-K. Hoi, X. Chen, V. S. Kumar, S. Homhuan, C.-H. Sow and A. A. Bettiol, *Adv. Funct. Mater.*, 2011, **21**, 2847.
4 K. Tsioris, G. E. Tilburey, A. R. Murphy, P. Domachuk, D. L. Kaplan and F. G. Omenetto, *Adv. Funct. Mater.*, 2010, **20**, 1083.
5 J. D. Joannopoulos, S. G. Johnson, J. N. Winn, R. D. Meade, in *Molding the Flow of Light*, Princeton University Press, Princeton, 2nd edn 2008.
6 K. Sakoda, in *Optical Properties of Photonic Crystals*, Springer, New York, 2nd edn 2005.
7 E. Yablonovic, *Phys. Rev. Lett.*, 1987, **58**(20), 2059.
8 S. John, *Phys. Rev. Lett.*, 1987, **58**(23), 2486.
9 G. von Freymann, A. Ledermann, M. Thiel, I. Staude, S. Essig, K. Busch and M. Wegener, *Adv. Funct. Mater.*, 2010, **20**, 1038.
10 M. van den Broek, L. A. Woldering, R. W. Tjerkstra, F. B. Segerink, I. D. Setija and W. L. Vos, *Adv. Funct. Mater.*, 2012, **22**, 25.
11 D. Erickson, D. Sinton and D. Psaltis, *Nat. Photonics*, 2011, **5**, 583.
12 X. Hu, Z. Li, J. Zhang, H. Yang, Q. Gong and X. Zhang, *Adv. Funct. Mater.*, 2011, **21**, 1803.
13 C. I. Aguirre, E. Reguera and A. Stein, *Adv. Funct. Mater.*, 2010, **20**, 2565.
14 Z. Wang, J. Zhang, J. Xie, C. Li, Y. Li, S. Liang, Z. Tian, T. Wang, H. Zhang, H. Li, W. Xu and B. Yang, *Adv. Funct. Mater.*, 2010, **20**, 3784.
15 C. J. Choi and B. T. Cunningham, *Lab Chip*, 2007, **7**, 550.
16 S.-K. Lee, S.-G. Park, J. H. Moon and S.-M. Yang, *Lab Chip*, 2008, **8**, 388.
17 S. Mandal, J.M. Goddard and D. Erickson, *Lab Chip*, 2009, **9**, 2924.
18 P. S. Nunes, N. A. Mortensen, J. P. Kutter and K. B. Mogensen, *Opt. Lett.*, 2008, **33**(14), 1623.
19 R. St-Gelais, J. Masson and Y.-A. Peter, *Appl. Phys. Lett.*, 2009, **94**, 243905–1.
20 G. Barillaro, S. Merlo, S. Surdo, L. M. Strambini and F. Carpignano, *Microfluid. Nanofluid.*, 2012, **12**, 545.
21 A. A. Yanik, M. Huang, A. Artar, T.-Y. Chang and H. Altug, *Appl. Phys. Lett.*, 2010, **96**, 021101–1.
22 Y. Guo, H. Li, K. Reddy, H. S. Shelar, V. R. Nittoor and X. Fan, *Appl. Phys. Lett.*, 2011, **98**, 041104–1.
23 P. S. Nunes, N. A. Mortensen, J. P. Kutter and K. B. Mogensen, *Sensors*, 2010, **10**, 2348.
24 E. Chow, A. Grot, L. W. Mirkarimi, M. Sigalas and G. Girolami, *Opt. Lett.*, 2004, **29**(10), 1093.
25 I. M. White and X. Fan, *Opt. Express*, 2008, **16**(2), 1020.
26 B. Wu, A. Kumar and S. Pamarthy, *J. Appl. Phys.*, 2010, **108**, 051101.
27 A. Lipson and E. M. Yeatman, *Opt. Lett.*, 2006, **31**(3), 395.
28 D. L. Kendall, *Annu. Rev. Mater. Sci.*, 1979, **9**, 373.
29 H. Seidel, *J. Electrochem. Soc.*, 1990, **137**(11), 3612.
30 S.-S. Yun, S.-K. You and J.-H. Lee, *Sens. Actuators, A*, 2006, **128**, 387.
31 A. Lipson and E. M. Yeatman, *J. Microelectromech. Syst.*, 2007, **16**(3), 521.
32 R. Mudachathi and P. Nair, *J. Microelectromech. Syst.*, 2012, **21**(1), 190.
33 M. Bassu, S. Surdo, L. M. Strambini and G. Barillaro, *Adv. Funct. Mater.*, 2012, **22**(6), 1222.
34 G. Barillaro, S. Merlo and L. M. Strambini, *IEEE J. Sel. Top. Quantum Electron.*, 2008, **14**(4), 1074.
35 G. Barillaro, L. M. Strambini, V. Annovazzi-Lodi and S. Merlo, *IEEE J. Sel. Top. Quantum Electron.*, 2009, **15**(5), 1359.
36 G. Barillaro, S. Merlo, S. Surdo, L. M. Strambini and F. Carpignano, *IEEE Photon. J.*, 2010, **2**(6), 981.
37 G. Barillaro, V. Annovazzi-lodi, M. Benedetti and S. Merlo, *Appl. Phys. Lett.*, 2007, **90**, 121110–1.
38 V. Lehmann and H. Föll, *J. Electrochem. Soc.*, 1990, **137**, 653.
39 J. V. Herràez and R. Belda, *J. Solution Chem.*, 2006, **35**, 1315.
40 G. Barillaro, S. Merlo and L. M. Strambini, *Opt. Lett.*, 2009, **34**(12), 1912.
41 G. Barillaro and F. Pieri, *J. Appl. Phys.*, 2005, **97**, 116105.
42 D. C. Angus, *Crit. Care Med.*, 2001, **29**, 303.
43 M. B. Pepys and M. L. Baltz, *Adv. Immunol.*, 1983, **34**, 141.
44 F. Baldini, *Sens. Actuators, B*, 2009, **139**, 64.